nature cell biology

LETTERS

https://doi.org/10.1038/s41556-018-0107-2

Regulation of cell cycle progression by cell–cell and cell–matrix forces

Marina Uroz[1], Sabrina Wistorf[1], Xavier Serra-Picamal[1], Vito Conte[1], Marta Sales-Pardo[2], Pere Roca-Cusachs[1,3], Roger Guimerà[2,4] and Xavier Trepat[1,3,4,5*]

It has long been proposed that the cell cycle is regulated by physical forces at the cell–cell and cell–extracellular matrix (ECM) interfaces[1–12]. However, the evolution of these forces during the cycle has never been measured in a tissue, and whether this evolution affects cell cycle progression is unknown. Here, we quantified cell–cell tension and cell–ECM traction throughout the complete cycle of a large cell population in a growing epithelium. These measurements unveil temporal mechanical patterns that span the entire cell cycle and regulate its duration, the G1–S transition and mitotic rounding. Cells subjected to higher intercellular tension exhibit a higher probability to transition from G1 to S, as well as shorter G1 and S–G2–M phases. Moreover, we show that tension and mechanical energy are better predictors of the duration of G1 than measured geometric properties. Tension increases during the cell cycle but decreases 3 hours before mitosis. Using optogenetic control of contractility, we show that this tension drop favours mitotic rounding. Our results establish that cell cycle progression is regulated cooperatively by forces between the dividing cell and its neighbours.

The growth of epithelial tissues enables development, wound healing and tissue regeneration[13,14]. During these processes, the regulation of cell proliferation is key to determine the shape, density and size of the growing tissue[15,16]. The regulation of the cell cycle by soluble chemical factors and intracellular molecular pathways has been the subject of extensive study for decades[17–19]. Early work also established that the shape and adhesion of a single isolated cell are potent regulators of DNA synthesis and cell growth[20,21]. However, the extent to which the duration of the cell cycle is directly regulated by cell size[22], nuclear size[23], growth rates[24], cytoskeletal tension[1] or by cell–ECM traction remains unclear.

Much less is known about the mechanical regulation of the cell cycle in cell collectives, such as epithelial and endothelial tissues. In these tissues, the shape and the size of the cell during the cycle are not only dependent on its growth but also on the forces and constraints imposed by its neighbours. Experiments using patterned two-dimensional (2D) and three-dimensional (3D) tissues established that spatial differentials in proliferation can be predicted by local tissue shape and mechanics[2,5,25]. More recently, exogenous stretching of epithelial layers was shown to stimulate progression from G1 to S[8] and from G2 to mitosis[10]. Later phases of the cell cycle, such as mitosis and cytokinesis have also been shown to be influenced by mechanical constrains[11], cell stretching[6] and by the mechanical action of neighbouring cells[9]. Taken together, these findings support the long-standing hypothesis that the cell reads out a force, a deformation or their rates to decide whether it progresses through or exits the cell cycle[7].

Despite the increasing evidence for the mechanical regulation of cell proliferation, the evolution of cell–cell and cell–matrix forces during the cell cycle has never been reported in an epithelium. Without this key information, the question of whether progression through the various phases of the cell cycle is mechanically driven remains unresolved. Here, we provide a systematic analysis of cell–ECM traction forces, cell–cell forces, as well as the cell and nuclear shape throughout the cycle of a large number of cells in an expanding epithelial monolayer. We show that cellular forces affect various phases of the cell cycle, including its duration, the G1–S transition and mitotic rounding.

As a model system for epithelial growth, we used the expansion of a micropatterned colony of MDCK cells. We placed a polydimethylsiloxane (PDMS) membrane with a 300-μm-wide rectangular opening on top of a collagen-I-coated polyacrylamide gel (11 kPa in stiffness)[26,27]. To monitor the cell cycle during growth of the colony, we seeded MDCK-Fucci cells on the pattern and allowed them to adhere and form a confluent monolayer. MDCK-Fucci cells express Ctd1-red fluorescent protein (RFP) during G1 and S phases and geminin-green fluorescent protein (GFP) during the S–G2–M phases, which allowed us to monitor the state of each cell in the cycle[6] (Fig. 1a,f). Four hours after seeding, the PDMS membrane was removed and cells migrated unidimensionally towards the newly available surface[26,27] (Fig. 1a and Supplementary Video 1). During the first hours of expansion, the monolayer flattened but no differences in height were observed between the leading edge and the bulk (Supplementary Fig. 1a–f). We used traction force microscopy to map traction forces at the cell–substrate interface[28] (Fig. 1b), and monolayer stress microscopy to map in-plane tension between and within cells[29] (Fig. 1c). Cell traction and tension increased during the first hours of expansion, as previously reported[27], but then decreased towards a plateau (Fig. 1d,e, Supplementary Fig. 2a–c and Supplementary Video 1). In parallel with collective migration, cells divided frequently across the monolayer (Supplementary Video 1). During the first ~12 h of expansion, the average cell area increased smoothly. The cell area then remained constant until the end of the experiment (Fig. 1g–i). By contrast, the average cell area in monolayers in which cell cycle progression was arrested with thymidine and aphidicolin showed a continuous growth, reaching a four-fold increase from the initial area (Fig. 1g–k and Supplementary Video 2). This result points to a mechanism by which MDCK

[1]Institute for Bioengineering of Catalonia (IBEC), The Barcelona Institute for Science and Technology (BIST), Barcelona, Spain. [2]Departament d'Enginyeria Química, Universitat Rovira i Virgili, Tarragona, Catalonia, Spain. [3]Unitat de Biofisica i Bioenginyeria, Facultat de Medicina, Universitat de Barcelona, Barcelona, Spain. [4]Institució Catalana de Recerca i Estudis Avançats (ICREA), Barcelona, Spain. [5]Center for Networked Biomedical Research on Bioengineering, Biomaterials and Nanomedicine (CIBER-BBN), Barcelona, Spain. *e-mail: xtrepat@ibecbarcelona.eu

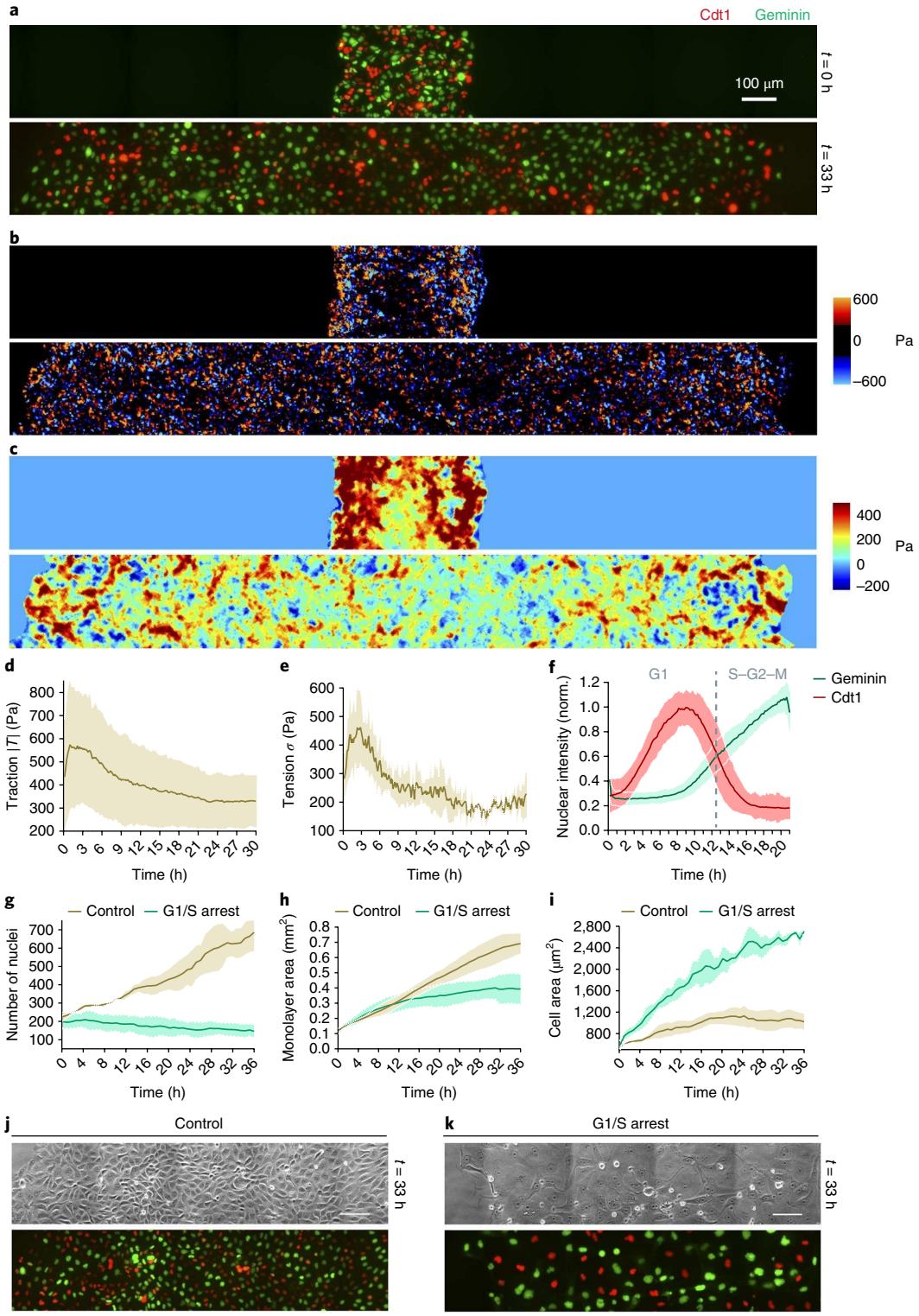

Fig. 1 | MDCK monolayers expand at a constant density. a–c, Fluorescence images of Fucci cells (**a**), tractions T_x (**b**) and tension σ (**c**) at 0 h and 33 h after removing the PDMS membrane. *t*, time. **d**,**e**, The monolayer mean traction modulus (**d**) and tension (**e**) during epithelial growth ($n = 3$ independent experiments). **f**, Normalized (norm.) fluorescence intensity of the green (geminin) and red (Cdt1) fluorescence channels ($n = 120$ cells from 3 independent experiments). The grey dashed line represents the transition point between G1 and S phases. For averaging, the time axis of each cell was interpolated to the average duration of the cycle. **g–i**, The mean number of nuclei (**g**), the monolayer area (**h**) and the area per cell (**i**) in monolayers expanding in control conditions and after arresting cells at the G1–S transition ($n = 3$ experiments per condition). **j**,**k**, Phase-contrast and fluorescence images 33 h after removing the PDMS membrane for the control (**j**) and the cell cycle arrest cases (**k**). Scale bars, 100 μm. All shaded areas in the graphs represent the s.d. Data in **a–c**,**j**,**k** are representative of $n = 3$ independent experiments.

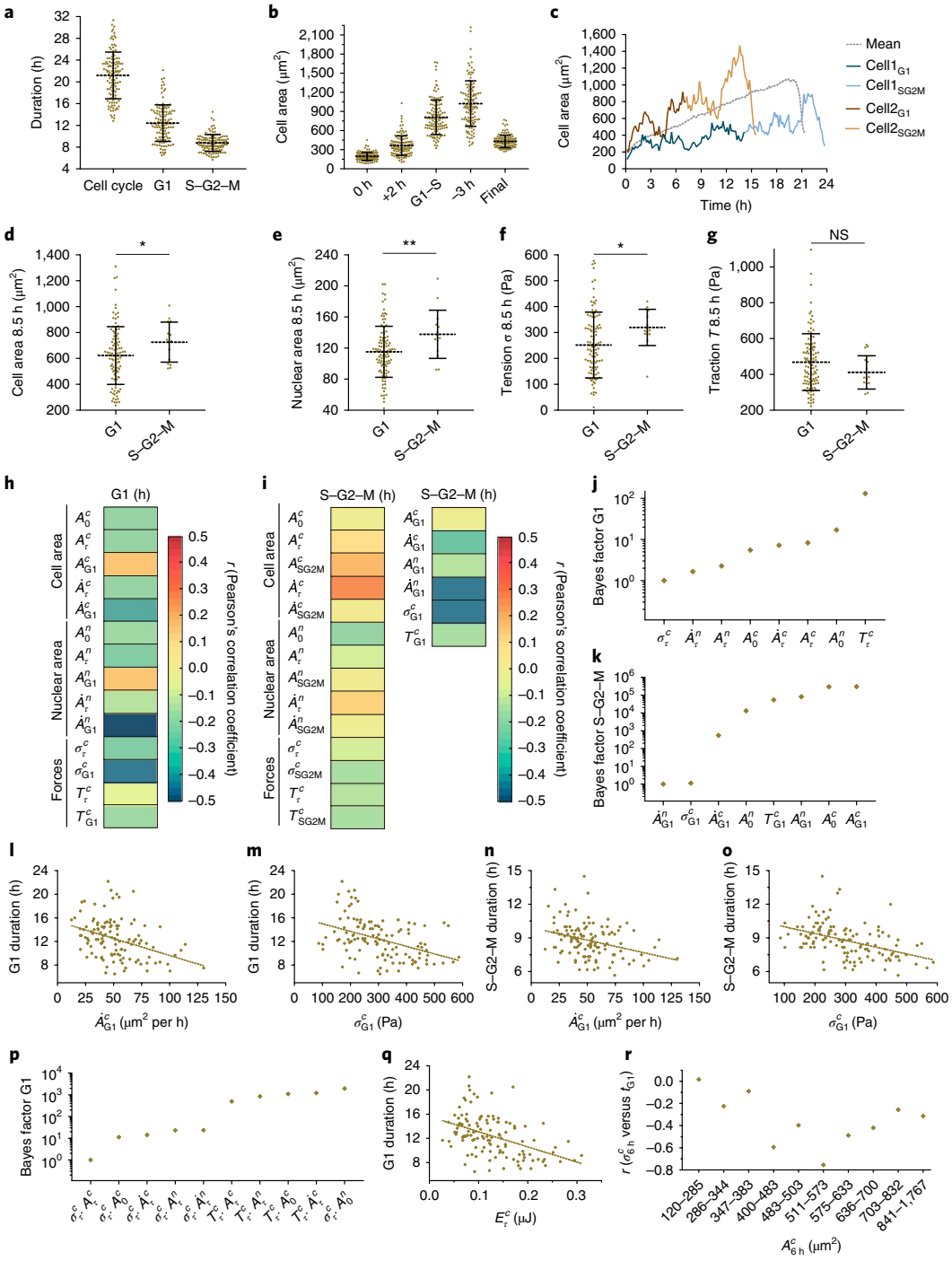

Fig. 2 | Cell tension and surface energy predict the duration of the cell cycle. a, The duration of the cell cycle, G1 and S–G2–M phases. **b**, The cell area at the beginning of the cycle (0 h), after 2 h, at the G1–S transition, 3 h before division and at the end of the cycle (final). **c**, Time evolution of the cell area for two representative cells (brown and blue). G1 and S–G2–M phases are labelled with different intensities. The dashed line represents the mean area for all the cells (for averaging, the time axis of each cell was interpolated to the average duration of the cycle). **d**–**g**, The mean cell area (*$P=0.048$) (**d**), the nuclear area (**$P=0.007$) (**e**), tension (*$P=0.013$) (**f**) and traction (not significant (NS), $P=0.227$) (**g**) for the cells in G1 and cells in S–G2–M 8.5 h after the beginning of the cycle (Mann–Whitney two-tailed test). **h**,**i**, Pearson's linear correlation coefficients between the durations of G1 (**h**) or S–G2–M (**i**) and the population-averaged cell properties. **j**,**k** Bayes factors of the predictive models that are linear in one property. A lower Bayes factor indicates higher plausibility (for example, if the Bayes factor of a model B with respect to the most plausible model A is 10, this means that model A is 10-times more likely than model B). Bayes factors of the linear models used to predict G1 durations from the averages of cell and nuclear properties over the first 6 h of the cycle are shown (**j**). Bayes factors of the linear models used to predict S–G2–M durations from the averages of cell and nuclear properties over G1 are shown (**k**). **l**,**m**, The G1 duration as a function of the mean cell area growth rate (**l**) and the mean tension (**m**) during G1. **n**,**o**, The S–G2–M duration as a function of the mean cell area growth rate (**n**) and the mean tension (**o**) during G1. **p**, Bayes factors of models that predict G1 durations and that are linear in the product of two properties. **q**, The G1 duration as a function of the mechanical energy. **r**, Pearson's linear correlation coefficients between the duration of G1 and cellular tension 6 h after the beginning of the cycle, σ^c_{6h}. Correlations are computed for each area decile 6 h after the beginning of the cycle, A^c_{6h}. All graphs include $n=120$ cells from 3 independent experiments. The dashed lines in **l**–**o**,**q** represent linear fits. The error bars in **a**,**b**,**d**–**g** represent the s.d and dotted lines represent mean.

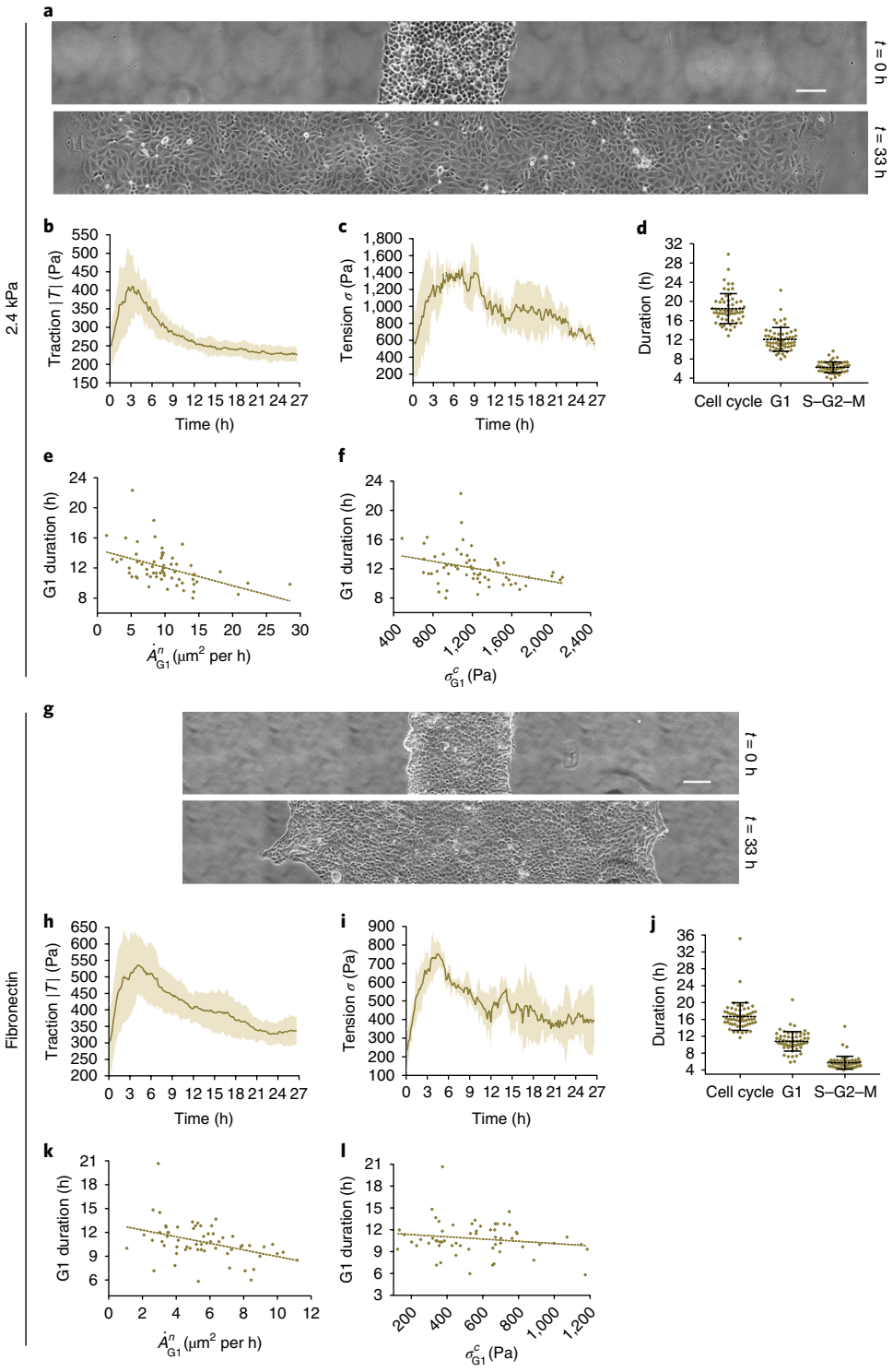

Fig. 3 | Tension and nuclear area growth rate correlate negatively with t_{G1} on softer substrates and on substrates coated with fibronectin. a, Phase-contrast images at 0 h and 33 h after removing the PDMS membrane. Images are representative of $n = 3$ independent experiments. Scale bar, 100 μm. **b**,**c**, The monolayer mean traction (**b**) and tension (**c**) during epithelial growth. **d**, The duration of the cell cycle, G1 and S–G2–M phases. **e**, The G1 duration as a function of the mean nuclear area growth rate during G1 ($r = -0.46$). **f**, The G1 duration as a function of the mean tension during G1 ($r = -0.34$). Panels **a**–**f** were in soft gels. **g**, Phase-contrast images at 0 h and 33 h after removing the PDMS membrane. Images are representative of $n = 3$ independent experiments. Scale bar, 100 μm. **h**,**i**, The monolayer mean traction (**h**) and tension (**i**) during epithelial growth. **j**, The duration of the cell cycle, G1 and S–G2–M phases. **k**, The G1 duration as a function of the mean nuclear area growth rate during G1 ($r = -0.41$). **l**, The G1 duration as a function of the mean tension during G1 ($r = -0.17$). Panels **g**–**l** were in fibronectin-coated gels. All graphs include $n = 60$ cells from 3 independent experiments. The error bars (**d**,**j**) and the shaded areas (**b**,**c**,**h**,**i**) represent the s.d. The dotted lines (**d**,**j**) represent the mean. The dashed lines in **e**,**f**,**k**,**l** represent linear fits.

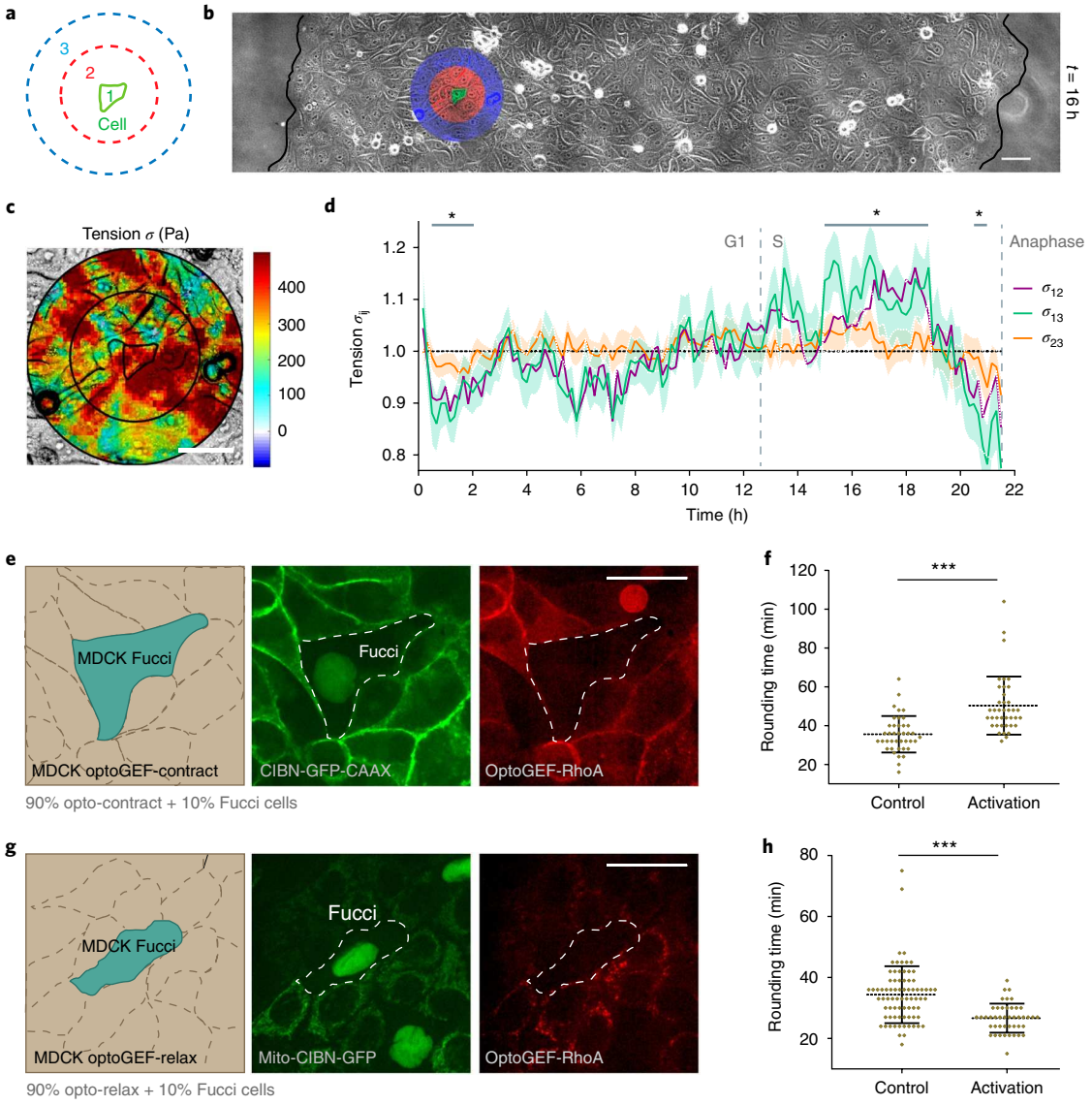

Fig. 4 | Cell tension increases during the cycle but decreases before mitosis. a, Illustration of the three ROIs used to average forces. **b**, A phase-contrast image highlighting the three ROIs for one representative cell (16 h after lifting the PDMS membrane). The black lines represent the monolayer outline. Scale bar, 100 µm. **c**, Tension overlapped on a phase-contrast image. The black lines indicate the contour of the three ROIs. Scale bar, 20 µm. **d**, The median of the tension ratios σ_{ij} ($n=120$ cells from 3 independent experiments). The time axis of each cell was interpolated to the average duration of the cycle. The grey dashed lines represent the transition between G1 and S and the beginning of anaphase. The shaded areas represent the s.e.m. for σ_{13} and σ_{23}. The s.e.m. for σ_{12} is not shown for clarity. The ratios σ_{ij} were averaged on the time points of interest (grey horizontal bars) to perform the statistical tests ($^*P=0.034$, $^*P=0.033$ and $^*P=0.026$, from left to right), using two-tailed Mann–Whitney test. The dashed horizontal line is a reference indicating a ratio of 1. **e**, Illustration of the experimental design to increase contractility in the neighbours of the dividing cell. A Fucci cell is surrounded by optogenetic MDCK optoGEF-contract cells (left panel). The green channel shows Fucci nuclei in G2 and CIBN-GFP-CAAX expressed in neighbouring cells (middle panel). The red channel shows neighbouring cells expressing optoGEF-RhoA (mCherry) (right panel). Scale bar, 30 µm. **f**, Rounding times of Fucci cells in the control case and under increased contractility of the neighbours (control: $n=40$ cells; activation $n=39$ cells from 3 independent experiments). $^{***}P<0.0001$, two-tailed Mann–Whitney test. **g**, Illustration of the experimental design to decrease contractility in the neighbours of the dividing cell. A Fucci cell is surrounded by optogenetic MDCK optoGEF-relax cells (left panel). The green channel shows the Fucci nuclei in G2 and mito-CIBN-GFP expressed in neighbouring cells (middle panel). The red channel shows neighbouring cells expressing optoGEF-RhoA (mCherry) (right panel). Scale bar, 30 µm. **h**, Rounding times of Fucci cells in the control case and under decreased contractility of the neighbours (control: $n=77$ cells; activation $n=44$ cells from 4 independent experiments). $^{***}P<0.0001$, two-tailed Mann–Whitney test. Images shown in **b**,**c**,**e** are representative of $n=3$ independent experiments. Images shown in **g** are representative of $n=4$ independent experiments. In (**f**,**h**) error bars represent s.d. and dotted lines lines represent the mean.

monolayers coordinate their growth and division cycle to maintain a constant cell density.

To investigate whether the duration of the cell cycle was mechanically regulated, we followed 120 cells from 3 independent monolayers throughout a complete cycle. The average duration of the cell cycle was 21.4 ± 0.4 h, of which 12.6 ± 0.3 h corresponded to G1 and 8.8 ± 0.1 h corresponded to S–G2–M (Fig. 2a). On average, the cell area exhibited a linear fivefold increase during the cycle, which resulted from both cell growth and spreading (Fig. 2b,c). We then asked whether a specific mechanical property promoted

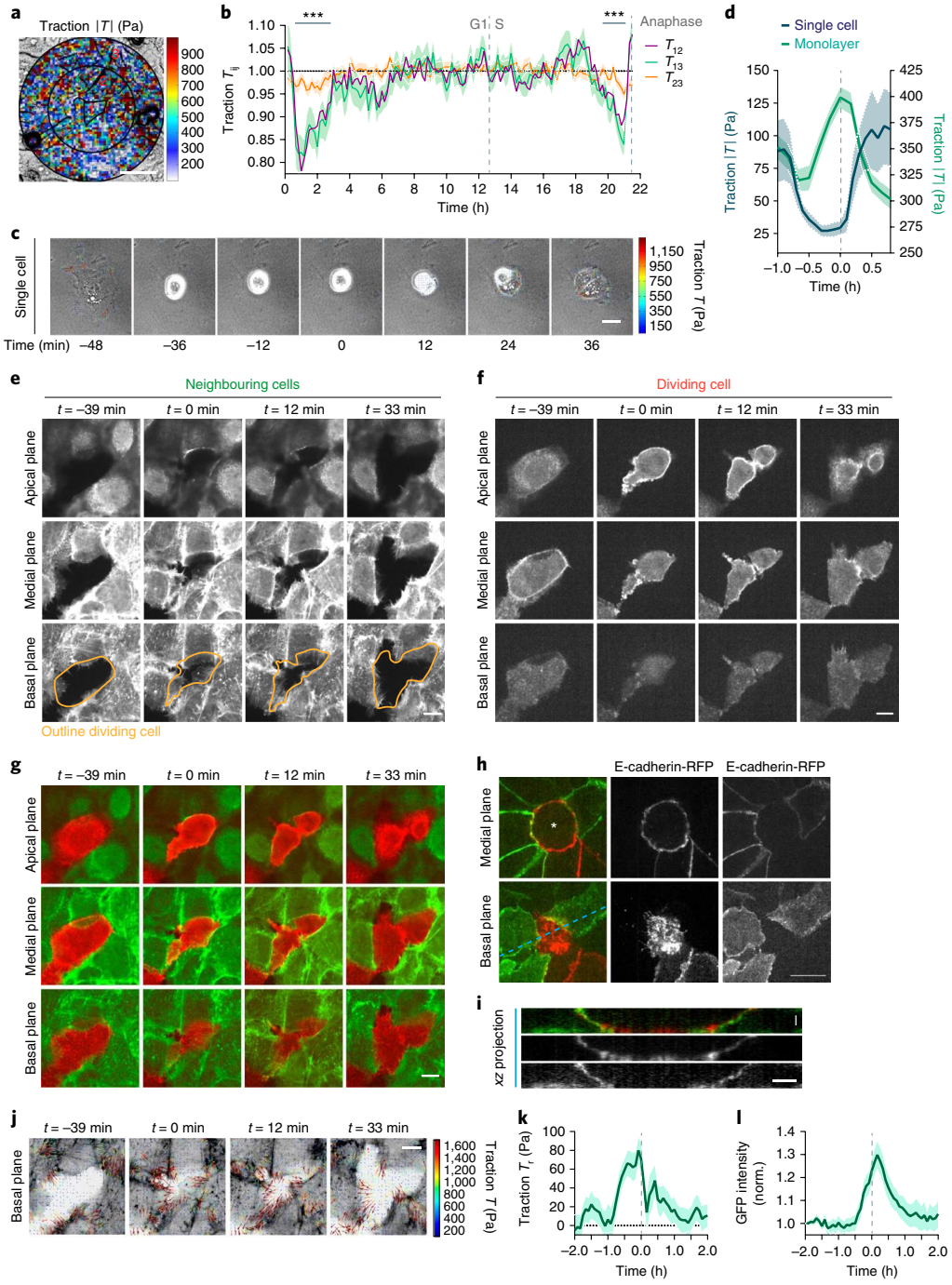

Fig. 5 | Neighbouring cells generate traction forces under the dividing cell during mitosis. a, Traction overlapped on a phase-contrast image. The black lines indicate the contour of the ROIs used to compute traction ratios T_{ij}. Scale bar, 20 µm. **b**, The median of the traction ratios T_{ij} ($n = 120$ cells from 3 independent experiments). The time axis of each cell was interpolated to the average duration of the cycle. The grey dashed lines represent the transition between G1 and S and the beginning of anaphase. The shaded areas represent the s.e.m. for T_{13} and T_{23}. The s.e.m. for T_{12} is not shown for clarity. The ratios were averaged on the time points of interest (grey horizontal bars) to perform the statistical tests (***$P = 0.0007$ and ***$P = 0.0009$ (from left to right), two-tailed Mann–Whitney test). The dashed horizontal line is a reference indicating a ratio of 1. **c**, Tractions during division of a single MDCK cell overlaid on phase-contrast images. The origin of the time axis (0 min) is defined as the last time point in which only one nucleus was visible. Scale bar, 20 µm. **d**, Time evolution of the mean traction during the division of a cell in isolation or in a monolayer. The dashed line represents the beginning of anaphase ($n = 120$ cells from 3 independent experiments for cells in monolayers and $n = 14$ cells from 3 independent experiments for isolated cells). The shaded areas represent the s.e.m. **e**,**f**, Basal, medial and apical fluorescence images of a dividing LifeAct-Ruby cell (**f**) surrounded by LifeAct-GFP cells (**e**). Scale bars, 10 µm. **g**, The merge of panels **e** and **f**. Scale bar, 10 µm. **h**, The projection of six medial and six basal planes of an E-cadherin-RFP cell in metaphase (asterisk), surrounded by E-cadherin-GFP neighbours. Scale bar, 22 µm. **i**, The *xz* projection for the cell in panel **h** along the blue dashed line. Merge (top), RFP (centre) and GFP (bottom) are shown. Scale bar: horizontal, 5 µm; vertical, 3 µm. **j**, Inverted LifeAct-GFP images corresponding to the basal planes shown in panel **e** with overlaid traction vectors. Scale bar, 10 µm. **k**,**l**, The mean radial traction (**k**) and the GFP normalized fluorescence (**l**) under LifeAct-RFP cells in expanding monolayers ($n = 40$ cells from 3 independent experiments). The dashed lines represent the beginning of anaphase. The dashed horizontal line is a reference indicating zero radial traction. The shaded areas represent the s.e.m. All images are representative of $n = 3$ independent experiments.

the transition from G1 to S. We reasoned that, if this was case, this mechanical property should be significantly different in cells that had transitioned to the S phase than in cells of the same age (defined as time elapsed since anaphase) that had remained in G1 (ref. [30]). To test this rationale, we focused on the time points at which only a small fraction of the cells had transitioned to the S phase, and plotted the average cell area, nuclear area, traction force and cellular tension for cells of the same age in the G1 and S phases. Cells that had transitioned to the S phase exhibited significantly higher cell and nuclear areas than those that had stayed in G1 (Fig. 2d,e). Tension was also higher in cells in the S phase than in identically aged cells in G1 (Fig. 2f). By contrast, traction forces did not show significant differences in G1 and S (Fig. 2g). This analysis is consistent with previous studies showing that cellular and nuclear spreading favour the G1–S transition[6,8], but it also raises the possibility that tension favours progression from G1 to S.

As geometric and mechanical properties might be linked, we sought to determine the extent to which each one of them predicts cell cycle progression. As potential geometric predictors, we considered the cell and nuclear areas shortly after the beginning of the cycle (A_0^c and A_0^n, measured 60 min after cell birth), as well as their average over the full period of G1 (A_{G1}^c and A_{G1}^n) and over the first τ hours of the cycle (A_τ^c and A_τ^n), where $\tau = 6$ h is the latest time point at which all cells remained in G1. We also considered the average rates of change of the cell and nuclear area over G1 ($\dot{A}_{G1}^c$ and $\dot{A}_{G1}^n$) and over τ ($\dot{A}_\tau^c$ and $\dot{A}_\tau^n$). Note that the volume and the mass were not experimentally accessible in our system and, therefore, growth rates reported in our study are changes in the 2D-projected areas of cells and nuclei. Given that cells are simultaneously growing and spreading, the relationship between area and volume is not straightforward[31,32]. As mechanical predictors, we considered traction force and tension averaged over G1 (T_{G1}^c and σ_{G1}^c) and over τ (T_τ^c and σ_τ^c).

We then tested whether these properties correlated with the duration of G1 (t_{G1}) (Fig. 2h and see Supplementary Fig. 3a,b for a complete correlation matrix between all of the measured properties). The cell and nuclear areas at the beginning of the cycle, as well as their time averages over τ and over the duration of G1 did not correlate with t_{G1} (Fig. 2h and Supplementary Fig. 4a–d). By contrast, the area growth rates of the cell and the nucleus correlated with t_{G1} with high significance ($P = 2\times10^{-5}$ and $P = 5\times10^{-13}$, respectively) (Fig. 2l). This result shows that cells that grow faster in an area divide earlier independently of their initial area. Importantly, tension also exhibited a high correlation with t_{G1} ($P = 2\times10^{-6}$) (Fig. 2m). This was not the case for traction forces (Fig. 2h). Similar results were obtained by averaging the mechanical properties between cell birth and the peak of the Ctd1 signal of each cell (Supplementary Fig. 3c,d). Tension and nuclear area growth rate also correlated negatively with t_{G1} on softer substrates (2.4 kPa) and, to a lesser extent, on substrates coated with fibronectin, thereby supporting the generality of our findings (Fig. 3). Overall, this correlation analysis shows that both mechanical and geometric properties are excellent candidates to explain t_{G1}.

To establish which of these properties is more predictive of t_{G1}, we carried out a model selection analysis[33,34]. This analysis compares a set of statistical models and selects those that are more plausible according to the Bayesian information criterion (BIC; see Methods). We first compared all models that are linear in one of the properties measured either at the beginning of the cycle or averaged over τ. We excluded properties averaged over the full length of G1 from this analysis, as these averages can include implicit t_{G1} and lead to trivial predictions. This analysis showed that tension was the most predictive property of t_{G1}, followed by nuclear area growth rate and nuclear area (Fig. 2j). Thus, if one has experimental access to all 2D geometric and mechanical properties over the first 6 h of the cycle, then the tension average of this period will be the best predictor of the duration of G1.

We also asked whether a combination of cellular properties could better predict t_{G1} than single properties. To do so, we tested all possible models involving the product of any pair of properties, irrespective of any a priori consideration with regard to their physical or biological meaning (Fig. 2p and Supplementary Fig. 5). Our analysis concluded that the product between cell area and tension outperforms the predictive power of any single property by more than one order of magnitude (Fig. 2p,q). The product of tension by area has units of energy and is related to the mechanical energy associated with the growth of the cell during the first τ hours of G1 (E_τ^c). A direct consequence of the predictive power of E_τ^c is that cells with the same area should enter G1 earlier if they are subjected to higher tension. To test this prediction, we ranked the 120 cells in area deciles and, for each decile, we computed the correlation between tension at 6 h and t_{G1} (Fig. 2r). With the exception of the first decile (the smallest cells), the correlation was always negative, confirming that, within a population of cells with the same area, those cells subjected to higher tension will progress faster in their cycle. This relationship cannot be explained through changes in cell height, as height and tension did not correlate for cells of the same area (Supplementary Fig. 1g–i). Finally, we explored all models that are multilinear on any pairwise combination of single properties and property products. None of these models had more predictive power than the best linear models of a single product of two properties (Supplementary Table 4).

We next carried out an analogous analysis asking whether mechanical properties during S–G2–M (labelled hereafter with the subscript SG2M) correlate with the combined duration of these phases of the cycle (t_{SG2M}). Unlike the case of G1, none of the mechanical properties measured during S–G2–M correlated with t_{SG2M} (Fig. 2i, left panel). By contrast, cell and nuclear area growth rates averaged over G1 correlated with t_{SG2M} ($P = 4\times10^{-4}$ and $P = 7\times10^{-7}$, respectively) and so did cellular tension ($P = 7\times10^{-7}$) (Fig. 2i, right panel and Fig. 2n,o). This result suggests that the S–G2–M phases have mechanical memory of G1, in the sense that they are influenced by the mechanical state of the cell during that earlier phase (Supplementary Fig. 3e). The analysis of linear models involving a single mechanical property showed that nuclear area growth rate and tension averaged over G1 were the best predictors of t_{SG2M} (Fig. 2k). Conversely, the analysis of models involving a product between pairs of properties showed that the product between nuclear area growth rate and tension during G1 was the most predictive (Supplementary Fig. 5). This product can also be interpreted in terms of energy because the average area growth rate during G1 and the area at the G1–S transition are highly correlated (Supplementary Fig. 4e–g). In summary, our statistical analysis shows that mechanical properties, such as tension and mechanical energy, are powerful predictors of the duration of the different phases of the cell cycle, outperforming geometric features, such as cell and nuclear areas and their rates of change.

To study in further detail the mechanical regulation of cell division, we focused on the time evolution of local tension during the full length of the cell cycle. For each time point, we averaged tension in three concentric regions around each cell of interest (Fig. 4a,b). The first region covers the area of the cell of interest (the green area in Fig. 4a,b), and the second and third regions are the two annuli that are consecutively concentric to that cell (the red and blue areas in Fig. 4a,b, respectively). To average out intercellular variability and to isolate variations associated with the cell cycle from global mechanical trends of monolayer expansion, we computed ratios of tension between pairs of regions (Fig. 4c). A tension ratio between regions i and j was then labelled as σ_{ij}, where indices i and j run from 1 to 3 (Supplementary Video 3). Throughout the cycle, σ_{23} was close to unity, indicating the absence of a systematic long-ranged tensional trend in the neighbourhood of the dividing cell (Fig. 4d). By contrast, σ_{12} and σ_{13} showed systematic departures from unity.

At the beginning of the cycle, σ_{12} and σ_{13} decreased slightly for ~1 h. Afterwards, they increased steadily through most of the cycle. Three hours before mitosis, σ_{12} and σ_{13} begun a progressive decrease and attained their minimum value at mitosis (Fig. 4d). σ_{13} dropped further than σ_{12}, indicating that tension in the immediate neighbours of the dividing cell decreased more than in distant cells.

This slow decline in tension suggests a regulatory mechanism that precedes mitosis. To investigate such a mechanism, we studied how mitosis is affected by tensional differences in the local environment of the dividing cell. To do so, we resorted to optogenetics to selectively increase or decrease tension in the neighbours of the dividing cell. We generated mosaic monolayers in which 10% of the cells expressed Fucci and the remaining 90% were engineered to either increase (MDCK optoGEF-contract) or decrease (MDCK optoGEF-relax) tension upon illumination with low doses of blue light[35] (Fig. 4e,g). When tension in the neighbours of a dividing cell was optogenetically increased, mitotic rounding slowed down (Fig. 4e,f). By contrast, when tension in the neighbours was decreased, rounding time accelerated (Fig. 4g,h). Previous work at the single-cell level showed that preventing mitotic rounding by placing an object in contact with a dividing cell delays mitosis and causes mitotic defects, such as spindle misassembly and pole splitting[11]. This delay was attributed to the need of the mitotic cell to generate an additional force to round up against the object. Our work suggests that increased tension in the neighbours of the mitotic cell also delays mitosis by preventing rounding. Thus, the drop in intercellular tension observed well before division might be a regulated process to ensure proper rounding and the absence of mitotic defects.

We next focused on the time evolution of traction ratios T_{ij} throughout the full length of the cell cycle (Fig. 5a,b). Unlike tension ratios, traction ratios T_{12} and T_{13} were constant during most of G1 and S–G2. This result is consistent with recent findings in single cells showing that tractions plateau between late G1 and S phases[12] (Fig. 5b). As cells rounded up for division, T_{12} and T_{13} exhibited a peak flanked by two periods of low traction (Fig. 5b,d). By contrast, single MDCK cells fully relaxed their tractions during rounding until re-spreading of daughter cells (Fig. 5c,d). To explore how tractions can develop under a rounding cell, we turned to mosaic monolayers in which 80% of the cells expressed LifeAct-GFP and the remaining 20% expressed LifeAct-Ruby. Confocal stacks revealed that neighbours of the dividing cell wrapped around it to maintain a largely continuous interface throughout mitosis[36,37] (Fig. 5e–g). During cytokinesis, the dividing cell and its neighbours co-ingressed and actin accumulated in the regions of the neighbours adjacent to the cleavage furrow[9](Fig. 5e and Supplementary Video 4). Imaging of the basal plane during division showed that, as the dividing cell detached from the substrate and rounded up, its neighbours extended cryptic actin-rich protrusions underneath it (Fig. 5e and Supplementary Video 4). The protrusions retracted after cytokinesis, thereby allowing daughter cells to spread. The time course of the protrusion–retraction cycle coincided with the generation of radial traction forces pointing away from the dividing cell (Fig. 5j–l). E-cadherin localized at the interface between the basal surface of the dividing cell and the apical surface of neighbouring protrusions (Fig. 5h,i and Supplementary Video 5). Together, these results raise the possibility that coordinated protrusion and retraction of neighbouring cells assists rounding of the mother cell and re-spreading of its daughters.

Cell mechanics has long been implicated in the regulation of cell proliferation[1–12,22,38], but how cellular forces evolve through the cell cycle and whether this evolution is associated with the duration of each of its phases have been unknown thus far. Here, we showed that cell–cell forces impact various phases of the cell cycle, including its duration, the G1–S transition and mitotic rounding. Furthermore, we showed that tension of the dividing cell relative to that of its surrounding neighbours increases smoothly through most of G1, S and G2. After an initial spreading phase, MDCK monolayers maintained a largely constant density, which suggests coordination between cell growth and division machineries during tissue expansion. This type of coordination has been observed in various tissues during development and homeostasis[19,31,39], which has led to the idea that cells read out their size to control progression through the cycle[6,24,30]. In the specific case of epithelial monolayers, previous experiments provided evidence that the G1–S and G2–M transitions are regulated by exogenous control of the cell area[6,8,10]. Here, we confirmed that the cell and nuclear areas, as well as their rates of change, predict progression through the cell cycle. More importantly, we found that tension and mechanical energy have a higher predictive power than geometrical properties; for a given cell area, cells under higher tension display a shorter G1. Taken together, these results point to distinct mechanisms by which cells probe an area and examine tension to progress through their cycle. The nature of these mechanisms and how they might be integrated to control the duration of G1, S and G2 are major questions that our study raises for future investigations.

Methods

Methods, including statements of data availability and any associated accession codes and references, are available at https://doi.org/10.1038/s41556-018-0107-2.

Received: 23 August 2017; Accepted: 23 April 2018;
Published online: 25 May 2018

References

1. Huang, S., Chen, C. S. & Ingber, D. E. Control of cyclin D1, p27^{Kip1}, and cell cycle progression in human capillary endothelial cells by cell shape and cytoskeletal tension. *Mol. Biol. Cell* **9**, 3179–3193 (1998).
2. Nelson, C. M. et al. Emergent patterns of growth controlled by multicellular form and mechanics. *Proc. Natl Acad. Sci. USA* **102**, 11594–11599 (2005).
3. Klein, E. A. et al. Cell-cycle control by physiological matrix elasticity and in vivo tissue stiffening. *Curr. Biol.* **19**, 1511–1518 (2009).
4. Mih, J. D., Marinkovic, A., Liu, F., Sharif, A. S. & Tschumperlin, D. J. Matrix stiffness reverses the effect of actomyosin tension on cell proliferation. *J. Cell Sci.* **125**, 5974–5983 (2012).
5. Aragona, M. et al. A mechanical checkpoint controls multicellular growth through YAP/TAZ regulation by actin-processing factors. *Cell* **154**, 1047–1059 (2013).
6. Streichan, S. J., Hoerner, C. R., Schneidt, T., Holzer, D. & Hufnagel, L. Spatial constraints control cell proliferation in tissues. *Proc. Natl Acad. Sci. USA* **111**, 5586–5591 (2014).
7. LeGoff, L. & Lecuit, T. Mechanical forces and growth in animal tissues. *Cold Spring Harb. Perspect. Biol.* **8**, a019232 (2015).
8. Benham-Pyle, B. W., Pruitt, B. L. & Nelson, W. J. Cell adhesion. Mechanical strain induces E-cadherin-dependent Yap1 and β-catenin activation to drive cell cycle entry. *Science* **348**, 1024–1027 (2015).
9. Pinheiro, D. et al. Transmission of cytokinesis forces via E-cadherin dilution and actomyosin flows. *Nature* **545**, 103–107 (2017).
10. Gudipaty, S. A. et al. Mechanical stretch triggers rapid epithelial cell division through Piezo1. *Nature* **543**, 118–121 (2017).
11. Lancaster, O. M. et al. Mitotic rounding alters cell geometry to ensure efficient bipolar spindle formation. *Dev. Cell* **25**, 270–283 (2013).
12. Vianay, B. et al. Variation in traction forces during cell cycle progression. *Biol. Cell* **110**, 91–96 (2018).
13. Park, S. et al. Tissue-scale coordination of cellular behaviour promotes epidermal wound repair in live mice. *Nat. Cell Biol.* **19**, 155–163 (2017).
14. Aigouy, B. et al. Cell flow reorients the axis of planar polarity in the wing epithelium of *Drosophila*. *Cell* **142**, 773–786 (2010).
15. Guillot, C. & Lecuit, T. Mechanics of epithelial tissue homeostasis and morphogenesis. *Science* **340**, 1185–1189 (2013).
16. Campinho, P. et al. Tension-oriented cell divisions limit anisotropic tissue tension in epithelial spreading during zebrafish epiboly. *Nat. Cell Biol.* **15**, 1405–1414 (2013).
17. Saxton, R. A. & Sabatini, D. M. mTOR signaling in growth, metabolism, and disease. *Cell* **169**, 361–371 (2017).
18. Yu, F. X., Zhao, B. & Guan, K. L. Hippo pathway in organ size control, tissue homeostasis, and cancer. *Cell* **163**, 811–828 (2015).
19. Lloyd, A. C. The regulation of cell size. *Cell* **154**, 1194–1205 (2013).

20. Folkman, J. & Moscona, A. Role of cell shape in growth control. *Nature* **273**, 345–349 (1978).
21. Watt, F. M., Jordan, P. W. & O'Neill, C. H. Cell shape controls terminal differentiation of human epidermal keratinocytes. *Proc. Natl Acad. Sci. USA* **85**, 5576–5580 (1988).
22. Chen, C. S., Mrksich, M., Huang, S., Whitesides, G. M. & Ingber, D. E. Geometric control of cell life and death. *Science* **276**, 1425–1428 (1997).
23. Roca-Cusachs, P. et al. Micropatterning of single endothelial cell shape reveals a tight coupling between nuclear volume in G1 and proliferation. *Biophys. J.* **94**, 4984–4995 (2008).
24. Son, S. et al. Direct observation of mammalian cell growth and size regulation. *Nat. Methods* **9**, 910–912 (2012).
25. Nelson, C. M., Vanduijn, M. M., Inman, J. L., Fletcher, D. A. & Bissell, M. J. Tissue geometry determines sites of mammary branching morphogenesis in organotypic cultures. *Science* **314**, 298–300 (2006).
26. Poujade, M. et al. Collective migration of an epithelial monolayer in response to a model wound. *Proc. Natl Acad. Sci. USA* **104**, 15988–15993 (2007).
27. Serra-Picamal, X. et al. Mechanical waves during tissue expansion. *Nat. Phys.* **8**, 628–634 (2012).
28. Trepat, X. et al. Physical forces during collective cell migration. *Nat. Phys.* **5**, 426–430 (2009).
29. Tambe, D. T. et al. Collective cell guidance by cooperative intercellular forces. *Nat. Mater.* **10**, 469–475 (2011).
30. Ginzberg, M. B., Chang, N., Kafri, R. & Kirschner, M. W. Cell size sensing in animal cells coordinates growth rates and cell cycle progression to maintain cell size uniformity. *bioRxiv* https://dx.doi.org/10.1101/123851 (2017).
31. Cadart, C. et al. An adder behavior in mammalian cells achieves size control by modulation of growth rate and cell cycle duration. *bioRxiv* https://dx.doi.org/10.1101/152728 (2017).
32. Guo, M. et al. Cell volume change through water efflux impacts cell stiffness and stem cell fate. *Proc. Natl Acad. Sci. USA* **114**, E8618–E8627 (2017).
33. Wagenmakers, E. J. A practical solution to the pervasive problems of *P* values. *Psychon. Bull. Rev.* **14**, 779–804 (2007).
34. Schwarz, G. Estimating the dimension of a model. *Ann. Stat.* **6**, 461–464 (1978).
35. Valon, L., Marin-Llaurado, A., Wyatt, T., Charras, G. & Trepat, X. Optogenetic control of cellular forces and mechanotransduction. *Nat. Commun.* **8**, 14396 (2017).
36. Reinsch, S. & Karsenti, E. Orientation of spindle axis and distribution of plasma membrane proteins during cell division in polarized MDCKII cells. *J. Cell Biol.* **126**, 1509–1526 (1994).
37. Higashi, T., Arnold, T. R., Stephenson, R. E., Dinshaw, K. M. & Miller, A. L. Maintenance of the epithelial barrier and remodeling of cell–cell junctions during cytokinesis. *Curr. Biol.* **26**, 1829–1842 (2016).
38. Burton, K. & Taylor, D. L. Traction forces of cytokinesis measured with optically modified elastic substrata. *Nature* **385**, 450–454 (1997).
39. Ginzberg, M. B., Kafri, R. & Kirschner, M. Cell biology. On being the right (cell) size. *Science* **348**, 1245075 (2015).

Acknowledgements

We thank N. Castro for technical assistance, A. Elosegui-Artola for assistance with the data analysis and L. Hufnagel for generously providing MDCK-Fucci cells. We are grateful to B. Baum and members of our groups for insightful comments and discussion. This work was supported by the Spanish Ministry of Economy and Competitiveness/FEDER (BES-2013-062633 grant to M.U., BFU2016-79916-P and BFU2014-52586-REDT to P.R.-C., BFU2015-65074-P to X.T., and BFU2016-75101-P and RYC-2014-15559 to V.C.), the Generalitat de Catalunya (2014-SGR-927 to X.T. and CERCA programme), the European Research Council (CoG-616480 to X.T.), European Commission (Grant Agreement SEP-210342844 to P.R.-C. and X.T.), Obra Social "La Caixa", a Career Integration Grant within the seventh European Community Framework Programme (PCIG10-GA-2011-303848 to P.R.-C.), Fundació la Marató de TV3 (project 20133330 to P.R.-C.). IBEC is recipient of a Severo Ochoa Award of Excellence from the MINECO.

Author contributions

M.U., X.S.-P. and X.T. conceived the study and designed the experiments. M.U. and S.W. performed the experiments. M.U. and X.S.-P. implemented the data analysis software. M.U. analysed the data. M.S.-P. and R.G. carried out the predictive model analysis. V.C. and P.R.-C. contributed data interpretation. All authors discussed the results. M.U. and X.T. wrote the manuscript with feedback from all authors. X.T. oversaw the project.

Competing interests

The authors declare no competing interests.

Additional information

Supplementary information is available for this paper at https://doi.org/10.1038/s41556-018-0107-2.

Reprints and permissions information is available at www.nature.com/reprints.

Correspondence and requests for materials should be addressed to X.T.

Publisher's note: Springer Nature remains neutral with regard to jurisdictional claims in published maps and institutional affiliations.

Methods

Cell culture. All MDCK cell lines were cultured in minimum essential media (MEM) with Earle's salts and L-glutamine (31095-029, Thermo Fisher) supplemented with 10% FBS (10270-106, Thermo Fisher), 100 units ml^{-1} penicillin, 100 µg ml^{-1} streptomycin and 292 µg ml^{-1} L-glutamine (10378-016, Thermo Fisher). Cells were maintained at 37 °C in a humidified atmosphere with 5% CO_2. The MDCK-Fucci stable cell line was a gift from L. Hufnagel[6]. For the optogenetic experiments, we used MDCK cells stably expressing CIBN-GFP-CAAX and optoGEF-RhoA and MDCK cells stably expressing mito-CIBN-GFP and optoGEF-RhoA[35].

Preparation of polyacrylamide gels. Glass-bottom dishes were activated by using a 1:1:14 solution of acetic acid/bind-silane (M6514, Sigma)/ethanol. The dishes were washed twice with ethanol and air dried for 5 min. For 11 kPa (2.4 kPa) gels, a 500 µl stock solution containing HEPES 10 mM, 93.75 µl (68.75 µl) acrylamide 40% (161-0140, Bio-Rad), 25 µl (11 µl) bisacrylamide 2% (161-0140, Bio-Rad), 2.5 µl 10% ammonium persulfate diluted in water (161-0700, Bio-Rad), 0.25 µl tetramethylethylenediamine (TEMED) and 12 µl of 200-nm-diameter far-red fluorescent carboxylate-modified beads (F8807, Thermo Fisher) was prepared. A drop of 18 µl stock solution was added to the centre of the glass-bottom dishes and the solution was covered with 18-mm-diameter GelBond film (Lonza) coverslips (hydrophobic side down) that were custom cut by an electronic cutting tool (Silhouette Cameo). After 40 min of polymerization, the coverslip was removed and gels were functionalized using sulfo-SANPAH. Briefly, a 80 µl drop of sulfo-SANPAH (22589, Thermo Scientific) was placed on the top of the polyacrylamide gel and activated by UV light for 3 min. Sulfo-SANPAH was diluted in miliQ water to a final concentration of 2 mg ml^{-1} from an initial dilution of 50 mg ml^{-1} kept at −80 °C. Gels were then washed twice with miliQ water and once with PBS for 5 min each. Afterwards, gels were incubated with 200 µl collagen I or fibronectin solution (0.1 mg ml^{-1}) overnight at 4 °C.

Microfabrication of the PDMS membranes. SU8-50 masters containing rectangles of 300 × 2,500 µm were fabricated using conventional photolithography. Uncured PDMS was spin coated on the masters to a thickness lower than the height of the SU8 feature (35 µm) and cured for 4 h at 60 °C. A thicker border of PDMS was applied at the edges of the membranes for handling purposes. PDMS was then peeled off from the master and kept in ethanol at 4 °C until use.

Cell patterning. Before seeding the cells, PDMS membranes were incubated in a solution of 2% Pluronic F-127 (Sigma-Aldrich) in PBS to prevent damage of the gel coating caused by the PDMS membranes. At the same time, the gels coated with collagen were washed twice with PBS, covered with cell media and kept in the incubator.

One hour after incubation of PDMS gels in 2% Pluronic solution, the membranes were washed twice with PBS and air dried for 20 min. After removing the media, the gels were air dried for 4 min. The PDMS membranes were then deposited on the surface of the gels and air dried for 2 min. A small volume (8 µl) containing 40,000 cells was placed on the exposed region of the polyacrylamide gel defined by the PDMS membrane. After 30 min, the unattached cells were washed off and 200 µl of medium were added. Four hours after seeding the cells (overnight for the gels coated with fibronectin), 2 ml of medium were added and the PDMS membranes were carefully removed with tweezers before starting the experiment. Time-lapse recording started approximately 1 h after removing the PDMS membrane. The interval between image acquisition was 10 min and a typical experiment lasted for 40 h. A row of 9 images was acquired for each pattern with a ×40 objective and then stitched with a MATLAB script.

G1/S cell cycle arrest. To arrest cells at the beginning of the S phase, a cocktail of 100 mM thymidine (T9250-1G, Sigma) and 5 mg ml^{-1} aphidicolin (A0781-1MG, Sigma) was added to the media of MDCK-Fucci cells 24 h before the start of the experiment (in the cell culture flask). The patterning procedure was identical to that of control cells, but cells were seeded with double the density to compensate for the lack of proliferation during 4 h of seeding. To quantify the number of nuclei, we used a custom-made MATLAB software based on a sequential thresholding of the image to capture nuclei with distinct levels of intensity. The cell area was computed by dividing the monolayer area by the number of nuclei.

Time-lapse imaging. Multidimensional acquisition routines were performed on an automated inverted microscope (Nikon Eclipse Ti) equipped with thermal, CO_2 and humidity control using MetaMorph/NIS Elements imaging software.

Spinning disk imaging. An inverted Nikon microscope with a spinning disk confocal unit (CSU-WD, Yokogawa) and a Zyla sCMOS camera (Andor) was used for high-resolution image acquisition.

Traction microscopy. Traction forces were computed using Fourier transform-based traction microscopy with a finite gel thickness[28]. Gel displacements between any experimental time point and a reference image obtained after monolayer trypsinization were computed using home-made particle imaging velocimetry software[28].

Monolayer stress microscopy. Monolayer stresses were computed using monolayer stress microscopy[29]. Monolayer stress microscopy uses traction forces and force balance demanded by Newton's laws to map the 2D stress tensor σ in the monolayer. By rotating these stress components at each point in the cell sheet, we computed the magnitude of the two principal stress components σ_{max} and σ_{min} and their corresponding, mutually perpendicular, principal orientations. For each point in the monolayer, we then computed the average normal stress within and between cells defined as $\sigma = (\sigma_{max} + \sigma_{min})/2$. This is the value reported in the paper as tension. Boundary conditions during migration were those described previously[27].

Monolayer height measurements. To measure the height of the monolayer while monitoring the state of the cell in the cycle, we used a MDCK cell line expressing Fucci and CIBN-CAAX-GFP. Z-stacks were acquired every 30 min using a ×60 oil objective. To image the full width of the monolayer, we tiled six fields of view in a row at every time point. To compute the monolayer height, we first divided the monolayer image in adjacent 14 × 14 µm (xy) square regions. We then averaged the intensity values in each region for each plane, thereby obtaining a profile of intensity in the z direction. We computed the monolayer height as the width at half-maximum of the z profile (that is, half of the distance between the maximum intensity and the background level). To report the xz profile shown in Supplementary Fig. 1f, we averaged the monolayer height in the y direction. The monolayer volume was calculated by integrating the monolayer height along the x and y axes.

Nucleus and cell shape tracking. To track individual cells within the monolayer, a custom-made MATLAB software was used. First, the position of the nucleus of interest was acquired manually in the frame before division, defined as the last frame in which one single nucleus could be distinguished. Then, proceeding backwards in time until the beginning of the cell cycle, each new position of the nucleus was obtained by (1) binarizing the images with a threshold (in a small region of interest (ROI) centred at the nucleus), (2) labelling the binarized nucleus and (3) overlapping the labelled image with a dilatation of the nucleus of interest in the previous analysed time point. The nucleus overlapping with the dilatation was defined as the nucleus of interest, and its position and mask were recorded. Finally, using the same method, but this time proceeding forwards in time and starting again in the division frame, the tracks of the two daughter nuclei during the first hour after division were obtained. In this case, each new region was centred between the two nuclei. After obtaining the nuclei tracks, a custom-made MATLAB software was used to manually draw the shapes of the cells during the cell cycle.

To define the G1–S transition time point, the mean fluorescence intensity in the nucleus was computed. Red and green channels were normalized separately (by the mean of the top 15% intensity values) and the transition time point was defined as the time point in which the two curves intersected. Using this procedure, 40 complete cycles (20 for the soft gel and fibronectin experiments) were analysed per experiment. All analysed cells started the cycle in the first 6 h of the experiment.

The nuclear and cell shape masks were used to compute the area and the area growth rate of the nucleus and the cell.

Averaging cell properties. All properties at each time point were obtained from the nuclear and cell shape masks. The initial areas A_0^c and A_0^n were defined as the area 60 min after the beginning of the cycle. For the prediction of t_{SG2M}, initial areas were defined as the area at the G1–S transition.

We defined the area growth rate at each time point i as:

$$\dot{A}_i = \frac{A_{i+1} - A_i}{t_{i+1} - t_i}$$

Traction and tension at each time point were defined as the mean of these properties over the cell area. For fibronectin coating and soft gel experiments, cell properties were averaged on a circle with a 24-µm radius centred at the cell nucleus.

Linear model selection analysis. To establish which properties are more predictive of the duration of the G1 and the S–G2–M phases, we carried out a systematic model comparison. In particular, we considered all models that are linear in one of the measured properties or in a product between two properties. We also explored all models that are multilinear on any pairwise combination of single properties and property products. To estimate the plausibility of each model, the BIC was used[34]. All models were compared to the most plausible one (that is, the model with the lowest BIC) using the Bayes factor, which is given by[33]:

$$\mathrm{BF}(A,B) = p(D|A)/p(D|B) \approx \exp\left[(\mathrm{BIC}(B) - \mathrm{BIC}(A))/2\right],$$

where p(D|A) is the probability of the observed data given model A. Thus, the Bayes factor (BF) gives the ratio between model plausibility (when all models are considered a priori equally plausible). For example, if the Bayes factor of a model B with respect to the most plausible model A is 10, this means that model A is 10-times more likely than model B.

Tension and traction ratios. To average forces in the three ROIs for each time point and cell, a custom-made MATLAB software was used. To average across the cell population, the time axis of each cell was linearly compressed or expanded so that the duration of G1 and S–G2–M was the average of all cells (G1 duration of 760 min and S–G2–M duration of 530 min). The ratios were then calculated for each cell and averaged afterwards.

Optogenetic experiments. The optogenetic system used here was described previously[35]. Briefly, the system is based on overexpressing a RhoA activator (the DHPH domain of ARHGEF11) fused to a light-sensitive protein, CRY2-mCherry. The resulting protein is called optoGEF-RhoA. Upon illumination, CRY2 changes conformation and binds to its optogenetic partner CIBN.

To increase contractility, optoGEF-RhoA was forced to localize at the cell surface, where RhoA is located, by targeting CIBN-GFP to the plasma membrane. To decrease contractility, optoGEF-RhoA was forced to localize at the mitochondria, by targeting CIBN-GFP to the mitochondrial membrane. Optogenetic experiments were performed using a stable MDCK cell line[35].

For experiments, the gels were air dried for 15 min after the media were removed. A drop of 10 µl containing a mixture of 90% optogenetic cells and 10% Fucci cells was deposited on top of the gel. After 30 min, 2 ml of media were added and the cells were left in the incubator overnight. The following day, dividing Fucci cells surrounded by optogenetic cells were imaged, both in activation and in control conditions. A laser of 488 nm was used to activate optogenetic cells. In the control case, time-lapse images were acquired using only brightfield (green light filtered) and a 561-nm laser. Cells were imaged for 8 h with time intervals of 3 or 4 min. Experiments were performed using a spinning disk microscope using a ×100 objective. Rounding time was defined as the time from nuclear envelope breakdown to anaphase.

Single-cell experiments. Single-cell imaging was acquired with ×40 objective with a timeframe of 6 min.

LifeAct imaging experiments. LifeAct experiments were performed by micropatterning the cells with the same protocol as the Fucci expansions but with a mixture of 80% LifeAct-GFP and 20% LifeAct-RFP cells instead. The interval between image acquisition was 5 min and a typical experiment lasted 15 h. Images were acquired with a ×40 objective. The shapes of dividing cells were acquired manually with a custom-made MATLAB software. Radial traction and green fluorescence were then averaged over time by using these masks. High-resolution LifeAct images were acquired with a spinning disk microscope and a ×60 objective.

Cadherin imaging experiments. Cadherin experiments were performed in glass, with spinning disk and a ×60 objective.

Statistics and reproducibility. Statistical comparisons were performed by using non-parametric Mann–Whitney test or Bayesian analysis, as indicated in each figure caption. All experiments were repeated three times except for experiments in Fig. 4g,h (repeated four times), Supplementary Fig. 1 (repeated four times) and Supplementary Fig. 2 (repeated two times).

Reporting Summary. Further information on experimental design is available in the Nature Research Reporting Summary linked to this article.

Code availability. The code used in this article can be made available upon request to the corresponding author.

Data availability. All data that support the findings of this study are available from the corresponding authors on reasonable request.